Coupled Design and Trajectory Optimization of an Electric UAV

Gonçalo Miguel Guardado Oliveira
goncalo.m.oliveira@tecnico.ulisboa.pt

Instituto Superior Técnico, Universidade de Lisboa, Portugal

June 2021

Abstract

In this work, coupled aircraft design and trajectory optimization is performed with the objective of producing a tailored UAV configuration and path that fulfil a mission at peak performance. The aerostructural component is handled by the OpenAeroStruct framework. This is a low-fidelity tool that uses a vortex-lattice method and a 1D finite-element analysis to model lifting surfaces. An upgrade of the framework is developed to accommodate propulsion and its performance metrics, as well as trajectory dependent computations. An electric propulsive system is considered where the propeller is modelled using a relation derived from Blade Element and Momentum Theory. A direct collocation method is used for the trajectory component. Gradient-based optimization is performed for different objectives, such as minimum energy consumed during climb, minimum time to climb to an arbitratry altitude, and maximum final distance starting from a cruise flight stage. The energy minimization problem is also optimized solely through trajectory or aircraft design, isolated, to better quantify the benefits of the coupled optimization. We verify that the coupled optimization is able to further minimize energy in 33% and 10.8%, relative to the isolated trajectory and aircraft design optimizations.

Keywords: Trajectory optimization, Aerostructural design, Multidisciplinary Design Optimization, Gradient-based optimization

1. Introduction

There has never been a wider range of aircraft. Different missions have different requirements that need adaptation of existing aircraft or even new solutions. The search for innovative and more advanced solutions that improve performance is what drives the development of new aircraft and the appearance of novel configurations. This is where aircraft design optimization comes in. An aircraft can be improved through the propulsive system, aerodynamics and/or structures. As for a mission objective, it can be further optimized through trajectory optimization. This consists in finding the best route and speed to complete the mission, whether it is simply going from A to B or heading to a certain zone and hovering around a target area. This part of the mission optimization is commonly done post design, so it is limited by the capabilities of the aircraft. Granted, the design is carried to satisfy some extreme flight limit conditions, but combining design and trajectory allows optimizing both configuration and mission to the fullest.

The aim of this work is to optimize trajectory and design simultaneously. The integration of disciplines is a key step in attaining this objective. To do so, we will resort to the OpenAeroStruct (OAS) framework [1], which will be responsible for handling the aerostructural analyses. This framework is upgraded to accommodate the implementation of electric propulsion and the trajectory component.

2. Background

2.1. Multidisciplinary Design Analysis and Optimization Tool

In this work, Multidisciplinary Design Analysis and Optimization (MDAO) is implemented through the OpenMDAO framework [2]. Its modular environment allows an easy integration of discipline analyses into a larger multidisciplinary model [2]. For the aerostructural disciplines in particular, the OpenAeroStruct (OAS) framework [1] is employed. It is a low-fidelity aerostructural analysis and optimization tool, developed in the OpenMDAO framework, that uses a Vortex-Lattice Method (VLM) and a 1D Finite-Element Method (FEM) to model lifting surfaces. The fluid-structure interaction (FSI) requires that the aerodynamic loads and structural displacements be transferred between the coupled analysis. The transfer scheme used in OAS satisfies the requirements of being consistent and conservative [1].

2.2. Structural Model

The equivalent spatial beam used in this work, depicted in Fig. 1, is a combination of truss, torsion and beam elements that model the behaviour due to axial, torsional and bending loads. Each spatial beam element has three translational and three rotational DOF for each of its two nodes. It is the result of the superimposition of four

elements: one bar with axial displacements, one torsion element with rotation about its longitudinal axis, and two beams with translational and rotational deformation (bending).

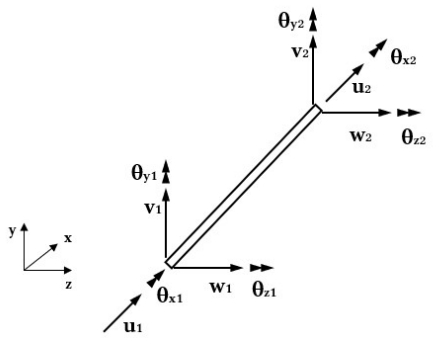

Figure 1: Spatial beam with 6 DOF per node. Adapted from [1].

The global stiffness matrix K is assembled and the system

$$K\boldsymbol{u} = \boldsymbol{F} \tag{1}$$

can be solved for the displacements $\boldsymbol{u}$, provided that the aerodynamic loads are known.

2.3. Aerodynamic Model

The lifting surface is divided in m trapezoidal panels of length l, as the one represented by the dashed line in Fig. 2. A horseshoe vortex is placed on each panel, with the bound vortex bc positioned at $\frac{1}{4}l$ and the trailing edge vortices ba and cd extending to infinity, all with the same strength Γ, as stated in Helmholtz's vortex theorems [3].

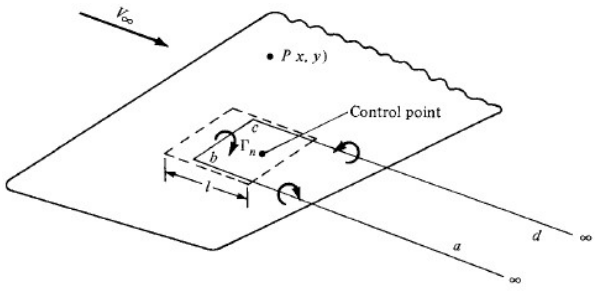

Figure 2: Representation of a horseshoe vortex [3].

The velocity induced by vorticity on a point P due to a segment $d\boldsymbol{l}$ of the horseshoe vortex with circulation strength Γ is expressed by the Biot-Savart law [3]. The induced component of velocity on a control point is influenced by each filament of every vortex system, including of its own panel. The total velocity is the sum of the freestream velocity and the total induced velocity and an impermeability condition is imposed on every control point, giving rise to the linear system

$$\boldsymbol{V}_\infty \cdot \boldsymbol{n}_k + \sum_{j=1}^{m} \Gamma_j (\boldsymbol{a}_{kj}^{ab} + \boldsymbol{a}_{kj}^{bc} + \boldsymbol{a}_{kj}^{cd}) \cdot \boldsymbol{n}_k = 0 \tag{2}$$

$$\iff A_{kj}\Gamma_j = -\boldsymbol{V}_\infty \cdot \boldsymbol{n}_k \tag{3}$$

where A is the aerodynamic influence coefficients matrix ($m \times m$).

Having solved this system for the circulation strengths, Kutta-Joukowski theorem is applied to compute the aerodynamic forces acting on each panel,

$$\boldsymbol{F}_k = \rho\Gamma_k(\boldsymbol{V}_\infty + \boldsymbol{v}_k) \times \boldsymbol{l}_k \tag{4}$$

where $\boldsymbol{v}$ is the velocity at the center of the bound vortex and $\boldsymbol{l}$ is the bound vortex vector.

2.4. Propulsion

Electric propulsive systems are a common solution for UAV applications because these systems are smaller and easier to integrate into aircraft of this size. It has other advantages, such as lower noise emissions, useful for stealth missions, and a much higher efficiency than that of combustion based systems.

Since one of the main goals is to perform trajectory optimization, it becomes necessary to model the propulsive system in a way that thrust is calculated explicitly, as well as the energy spent.

The energy density of the battery is 210 Wh/Kg and the available electric power is assumed constant and superior to the power drawn by the motor.

It is assumed that the electric motor has a constant maximum power of 180 W, and the actual power is controlled by a throttle setting δ_T, such that

$$P_m = \delta_T P_{Max}, \quad \delta_T \in [0, 1]. \tag{5}$$

The loss factor is given by

$$LF = \frac{P_m}{P_e} \tag{6}$$

and assumed constant with a value of 50%.

The mechanical power that the motor transmits to the shaft is converted by the propeller into thrust force, which is calculated using a result of Blade Element and Momentum Theory [4]

$$P_{disk} = TV_\infty + \frac{\kappa}{2}T\left(-V_\infty + \sqrt{V_\infty^2 + \frac{2T}{\rho A_{disk}}} \right). \tag{7}$$

P_{disk} is the power supplied to the propeller disk, here assumed equal to P_m, T is the thrust, V_∞ is the freestream velocity, ρ is the air density and A_{disk} is the disk area of the propeller. The correction factor κ accounts for induced-power losses related to non-uniform inflow, tip effects, and other simplifications made in momentum theory [5]. It is assumed $\kappa = 1.2$,

where the ideal is 1. The disk area is calculated by $A_{disk} = \pi \frac{d^2}{4}$, where the disk diameter d is 30 cm.

The combination of the models of the propulsion components yields a simple algorithm for the propulsive system. The mechanical power, controlled by the throttle setting δ_T, is calculated through Eq. (5). This mechanical power and air speed are inputs to Eq. (7), from which thrust is explicitly calculated using the Newton-Raphson method. The electrical power is obtained from the loss factor Eq. (6) and is then used to calculate the electrical energy spent

$$E_e = \int P_e dt, \tag{8}$$

which is limited by the energy of the battery

$$E_e \leq E_{bat} = m_{bat} e. \tag{9}$$

2.5. Aircraft Dynamics

Three reference frames are used. The aircraft frame $\mathcal{F}_A(x', y', z')$ has its origin at the center of mass of the aircraft and moves with it. The x' axis is the aircraft's longitudinal axis and the z' axis is perpendicular to it, pointing upwards; The flight path frame $\mathcal{F}_P(x, y, z)$ also has its origin in the centre of mass of the aircraft and moves with it. It differs from the aircraft frame in that the x axis is aligned with the airspeed vector $\boldsymbol{V}_\infty$; Finally, the inertial Earth frame is designated by $\mathcal{F}_E(x_E, y_E, z_E)$. The Earth is assumed non-rotating and its curvature is neglected, so the origin is on the ground, the x axis is aligned with the local horizon and the z axis is normal to it pointing upwards, so the gravitational acceleration $\boldsymbol{g}$ is negative.

In this work, only the longitudinal component of flight is considered, so it is assumed there is no rotation about the x and z axis and no translational motion along y. Wind speed and sideslip angle (β) are also assumed to be zero. The forces acting on the aircraft are the gravitational force, $\boldsymbol{W} = m\boldsymbol{g}$, where m is the mass, the aerodynamic forces lift ($\boldsymbol{L}$) and drag ($\boldsymbol{D}$), and the propulsive force, thrust $\boldsymbol{T}$. They are represented in Fig. 3(a).

The derivation of the equations of motion in the Earth frame starts with Newton's second law relative to the translation of the center of mass. Writing the forces in the two components of the Earth frame yields

$$\sum F_{x_E} = T\cos(\alpha + \gamma) - D\cos(\gamma) - L\sin(\gamma) = m\ddot{x} \tag{10}$$

$$\sum F_{z_E} = L\cos(\gamma) + T\sin(\alpha + \gamma) - W - D\sin(\gamma) = m\ddot{z}. \tag{11}$$

Since flight is considered two dimensional and both the flow and the aircraft are symmetric over the longitudinal axis, there is only pitching moment. It is assumed that thrust is parallel to x' and aligned with the center of mass, so $\boldsymbol{r}_T \times \boldsymbol{T} = 0$. Additionally, the aircraft is considered to always be in a state of equilibrium of moments, as the time and spatial scales considered are large enough for the non stationary terms to be neglected,

$$\boldsymbol{M}_y = \boldsymbol{M}_w + \boldsymbol{r}_w \times \boldsymbol{L}_w + r_w \times \boldsymbol{D}_w + \boldsymbol{M}_t + \\ + \boldsymbol{r}_t \times \boldsymbol{L}_t + \boldsymbol{r}_t \times \boldsymbol{D}_t = 0. \tag{12}$$

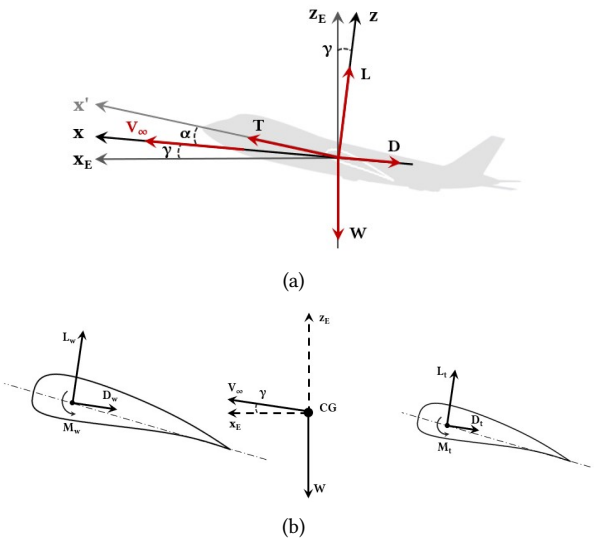

Figure 3: (a) Representation of the forces acting on the aircraft's center of mass. (b) Simplified representation of the moments about the center of mass of the aircraft.

2.6. Trajectory

Numerical methods for solving optimal control problems are divided into three major methods: dynamic programming, indirect methods and direct methods.

Direct methods can deal with large systems, are more robust, flexible and not as difficult to construct and solve, because they do not require the analytical derivation of the necessary conditions [6]. With this approach, the OCP is reduced to a nonlinear programming (NLP) problem.

Transcription is the first step for obtaining the NLP. Direct transcription refers to the transformation of the infinite dimensional continuous part of the OCP into a finite dimensional NLP [6], which is done through the parameterization of the state and/or control. Direct collocation is the method used for state and control parameterization.

Focusing on local collocation, the number of collocation points in a given subinterval is fixed and the number of subintervals is varied [7]. Time is broken into N subintervals, $h_i = t_{i+1} - t_i$, $(i = 0, \ldots, N-1)$ and the dynamics of the system, ruled by the differential equations,

$$\dot{\mathbf{s}}(t) = \boldsymbol{f}(\mathbf{s}(t), \mathbf{u}(t)), \tag{13}$$

are not integrated sequentially to obtain the state $\mathbf{s}_{i+1}$, like in shooting methods. Instead, they function as defect constraints,

$$\zeta = \dot{\mathbf{s}}(t) - \boldsymbol{f}(\mathbf{s}(t), \mathbf{u}(t)) = 0, \tag{14}$$

imposed on each collocation point to ensure consistency between state and control values throughout the trajectory. Equation (14) can be discretized using Runge-Kutta or orthogonal methods.

Collocation has the advantage of avoiding sequential integration. As a result, errors are not propagated and computational costs are reduced. However, that is done by adding design variables and constraints, thus giving up the simpler NLP and low number of variables of shooting methods. This may lead to more function evaluations, more gradients to be computed and significant increase in memory needed for storing the Hessian matrix [6].

In this work, a collocation method is implemented, where the dynamics are represented by equations (10) and (11) and discretized with forward Euler method, yielding the collocation constraints

$$\zeta_{F_x} = \sum \boldsymbol{F}_{x_E} - m\ddot{x} = 0 \iff \sum F_{x_E,i} - m\frac{\dot{x}_i - \dot{x}_i}{\Delta t} = 0 \quad (15)$$

$$\zeta_{F_z} = \sum \boldsymbol{F}_{z_E} - m\ddot{z} = 0 \iff \sum F_{z_E,i} - m\frac{\dot{z}_i - \dot{z}_i}{\Delta t} = 0 \quad (16)$$

$$\zeta_x = \dot{x}_i - \frac{x_{i+1} - x_i}{\Delta t} = 0 \quad (17)$$

$$\zeta_z = \dot{z}_i - \frac{z_{i+1} - z_i}{\Delta t} = 0. \quad (18)$$

The collocation method was chosen for the advantages aforementioned and because of its easier integration into the OpenAeroStruct framework, as will be explained in section 3.1.

3. Implementation

3.1. Framework Implementation

Multidisciplinary Analysis (MDA) is performed to find a solution that satisfies the systems of equations that represent the coupled system, which comprises the repeated evaluation of the target and response states until they are equal. The solver employed in this work is NLBGS with Aitken's relaxation, as it has better convergence with increasing coupling strength [1].

The MDO architecture implemented in this work is a variation of MDF and its extended design structure matrix (XDSM) [8] is shown in Fig. 4. Like in the usual MDF, the task of computing each discipline's states is handled by the MDA, which does so by running a fixed point iterative solver. In this case, the coupled analysis are structures and aerodynamics, coupled through the loads and mesh displacements states, and subject, among other, to the flow variables. These flow variables, such as air density and velocity, result from the trajectory (or are prescribed for the isolated design problem) and therefore may vary from one flight point to another. Therefore, the fluid-structure interaction needs to be solved for every point of the trajectory discretization.

OpenAeroStruct has a multipoint feature that allows optimizing the aircraft design for several flight conditions. However, is not done in a vectorized way. Instead, a new "mission point" is created for each set of flight conditions and a new MDA is called to solve the FSI.

The trajectory variables are inputs to the Preprocessing component, where the flow variables are computed and then forwarded to Aerodynamics and Point Performance components. The Structures component receives the geometric variables, which are the same for all MDAs, and the correspondent entry of the stabilator angle vector. The Aerodynamics component receives the angle of attack. The MDA is run until convergence is achieved and once it does, thrust and energy spent during the mission point are calculated in the Propulsion component.

The thrust force, the final load distribution, the structural mass and surface areas are inputs to the Point Performance component, where a series of functions are computed to obtain lift and drag coefficients, total weight, center of mass and moments. All these intermediate computations are necessary to calculate the values of failure, material intersection and moments coefficient constraints, which are then evaluated by the optimizer. They are also necessary to compute the sum of forces that are then passed to Mission Performance, in order to get the value of the collocation constraints. The energies of all mission points, calculated in Propulsion, are summed in Mission Performance to obtain the total energy spent and the energy constraint value.

MDAs are independent from each other and there is no data flow between them. This is a consequence of having chosen a collocation method. Since states and control are handled directly by the optimizer, variables dependent on trajectory and control can be vectorized and only the correspondent entries are passed to each MDA.

This framework implementation results in two very distinct philosophies for FSI and trajectory. The FSI part of the optimization is carried through a solver-based approach, in which the governing equations are solved, whereas trajectory is handled directly by optimizer, with the states are design variables chosen so that the associated constraints are satisfied.

4. Results

4.1. Baseline Problem Definition

The optimizer used is SLSQP, as gradient based methods perform better and this is the best open source option [9]. The optimizer tolerance is 10^{-3} and the solver's absolute and relative tolerances are 10^{-7} and 10^{-30}, respectively.

A mesh convergence study was performed to determine the number of panels that yields accurate results with acceptable computational time and effort. To do so, one MDA was converged for several (num_x, num_y) pairs and the computation times and resultant

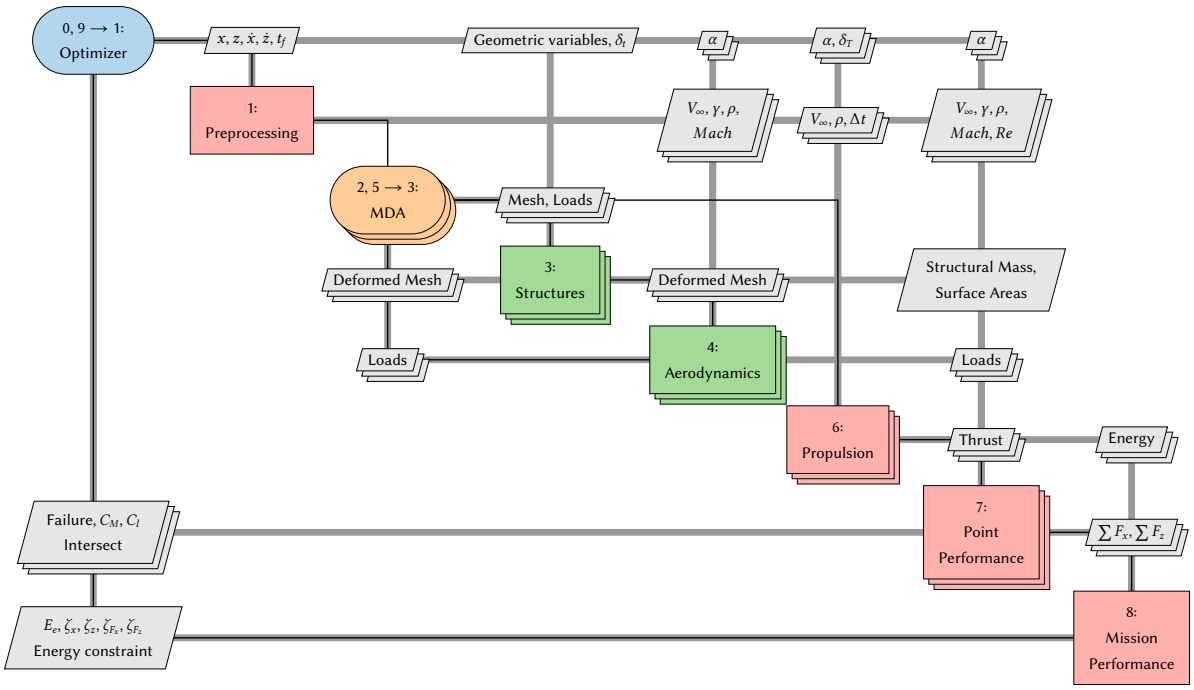

Figure 4: Extended design structure matrix (XDSM) of the architecture implemented.

drag coefficients C_D of an arbitrary wing shape and flow were compared. It was found that the variation of C_D relative to the previous result was negligible for 6×30 panels for the wing. for the tail, a panel ratio of 3 is applied: 4×12.

The initial aircraft configuration is based on the mini-UAV Tekever AR4 [10]. Due to limited available technical data on this aircraft, many parameters were deduced. The constant parameters of the aircraft are shown in Tab. 1, and the control and trimming variables, initialized with the same value for all mission points, are shown in Tab. 2. The complete list of design parameters and their bounds is presented in Tab.4.

Table 1: UAV constant parameters.

Parameter	Wing	Tail	Units
C_{L_0}	0.2434	0	-
C_{D_0}	0.00860	0.00852	-
max (h/c)	10	10	%
max (h/c) position	30	30	%
	Global		
Empty CG	-0.2, 0, 0		m
Empty mass, m_0	1.2		kg
Battery mass, m_{bat}	1.5		kg
Specific energy, e	210		Wh/kg
Loss factor, LF	50		%
Max motor power, P_m	180		W
Propeller radius, r	0.15		m
Induced-power loss factor, κ	1.2		-

Table 2: UAV trimming and control parameters.

Parameter	Initial Value	Bounds	Units
Throttle, δ_T	0.5	0, 1	
Angle of attack, α	4	-15, 15	degrees
Stabilator angle, δ_t	-0.2	-10, 10	degrees

The material composition of the AR4 is unknown, so we simplified and considered that the spar tube is made of aluminum 6061, being the mechanical properties listed in Tab. 3. A safety factor of 2 is applied to the yield strength. The spar is placed at 30% of the chord in both surfaces, which is the point where thickness over chord ratio (h/c) of the airfoil is greatest.

Table 3: Mechanical properties of aluminum 6061 [11].

Parameter	Value	Units
Young's modulus, E	69	GPa
Yield strength, σ_{yield}	276 / 2	MPa
Density, ρ	2700	kg/m^3
Poisson's ratio, ν	0.33	-

The trajectory is discretized into $N = 10$ intervals. The initial position is $(x, z) = (0, 0)$ m, assuming that the UAV is launched at ground level, and the initial velocity is 14 m/s. After this point, the velocity is kept at 15 m/s until the final altitude (1000 m) is reached and the total flight time is 570 seconds. Horizontal and vertical displacement variables are both bounded by $[0, 100000]$ m.

Table 4: Initial values and bounds of UAV design variables.

Parameter	Wing		Tail		
	Initial Value	Bounds	Initial Value	Bounds	Units
Span, b	2.1	1.2, 2.6	0.42	0.25, 0.6	m
Chord cp, c	0.18, 0.25	0.1, 0.3	0.14, 0.17	0.08, 0.21	m
Twist cp, θ	1.5, 1.5, 1.5	-20, 20	0	0	degrees
Dihedral, $\urcorner$	4	-20, 20	0	-20, 20	degrees
Sweep, Λ	1.5	-20, 20	0.5	-20, 20	degrees
Thickness cp, t	0.003, 0.003, 0.003	0.0015, 0.05	0.0025, 0.0025, 0.0025	0.0015, 0.04	m

Velocity's horizontal component is bounded by $[0, 18]$ m/s and the vertical by $[-18, 18]$ m/s. Flight path angle γ varies as shown in Fig. 5.

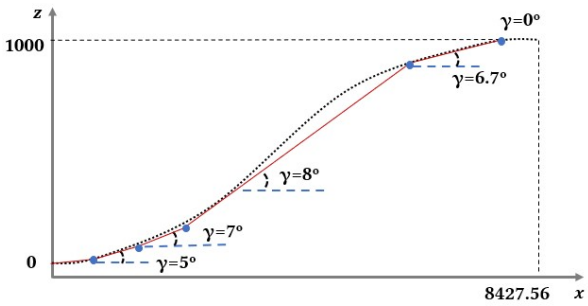

Figure 5: Discretization of the initial climb trajectory.

4.2. Optimal Design for Minimum Energy Climb

The energy consumed during climb was minimized through trajectory (TP), aircraft design (DP), and through both, simultaneously (DTP). The initial aircraft configuration just presented was the same for the three problems, being fixed for TP. Likewise, the initial trajectory was also the same and fixed for DP. The three problems are defined in Tab. 6.

Optimization was successfully concluded with the computational costs shown in Tab. 5.

Table 5: Optimization performance with an Intel® Core™ i7-5500 @ 2.4 GHz Processor.

Parameter	TP	DP	DTP
Iterations	17	20	74
Function evaluations	22	81	171
Computation time	2h23	2h41	11h28

DTP uses all 94 design variables and 302 constraints. DP only optimizes design, so trajectory variables and collocation constraints pertaining to displacement ζ_x, ζ_z are not used, which gives 49 design variables and 282 constraints. TP does not include any geometric variables nor the intersection constraints, which amounts to 75 design variables and 281 constraints. The Hessian sizes are given by the square of the sum of design variables and constraints. They are 126736, 109561 and 156816, for TP, DP and DTP, respectively.

DTP is a considerably larger problem, so it is natural that its optimization took longer. Its Hessian is 43% larger than DP's, and 24% larger than TP's. DP is a smaller problem than TP, yet it took more function evaluations and time. One possible explanation might be the handicap that a prescribed trajectory represents, and the difficulty of adapting a design to it. Another possible explanation might lie in fact that DP has less variables for almost the same number of constraints than TP. This results in a more rigid problem, as the optimizer has fewer variables to try to satisfy approximately the same number of constraints, which makes it harder to find a solution. Moreover, DP and DTP deal with optimization of the aerostructural component, which becomes increasingly harder to converge as coupling strength increases.

The optimal solutions found are shown in Tab.7, Figures 6, 7 and 8.

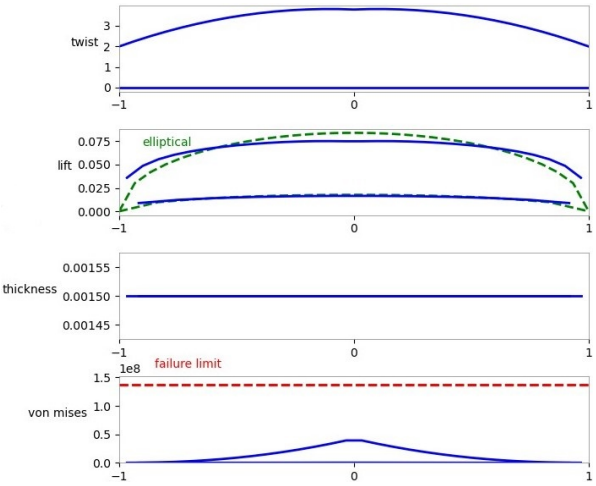

Figure 6: Twist, lift, thickness and stresses distribution along span for Design + Trajectory problem.

As seen in Tab. 7, DTP had the least amount of energy spent E_e, with a reduction of 33% relative to TP, and 10.8% relative to DP. TP and DP are limited by the prescribed trajectory and configuration, respectively, whereas in DTP, the optimizer has access to both design and trajectory variables and therefore, produces

Table 6: Formulation of the three optimization problems.

	Parameter	Note	Quantity		
			TP	DP	DTP
Minimize	E_e		1	1	1
W.r.t					
Geometry	θ_w, t_w, t_t	3 control points	0	9	9
	c_w, c_t	2 control points	0	4	4
	$b_w, b_t, \Lambda_w, \Lambda_t, \urcorner_w, \urcorner_t$		0	6	6
Trajectory	$x, \dot{x}, z, \dot{z}$	vectors of size N+1	44	0	44
	t_f		1	0	1
Control	$\delta_T, \alpha, \delta_t$	vectors of size N	30	30	30
		Total	**75**	**49**	**94**
Subject to					
Collocation	$\zeta_x, \zeta_z, \zeta_{F_x}, \zeta_{F_z} = 0$	vectors of size N	40	20	40
Equilibrium	$C_{M_y} = 0$	vector of size N	10	10	10
Aerodynamic	$C_{l_w} < Cl_{w_{max}}$	vector of size $\frac{num\_y-1}{2} \times N$	150	150	150
	$C_{l_t} < Cl_{t_{max}}$	vector of size $\frac{num\_y-1}{2} \times N$	60	60	60
Structural	$Intersect_w < 0$	vector of size $\frac{num\_y-1}{2}$	0	15	15
	$Intersect_t < 0$	vector of size $\frac{num\_y-1}{2}$	0	6	6
	$Failure_w, Failure_t < 0$	$N\times$ KS function	20	20	20
Energy	$E_e \leq E_{bat}$		1	1	1
		Total	**281**	**282**	**302**

Table 7: Final values of geometric design variables for TP, DP and DTP problems.

	Parameter	Trajectory	Design	Design + Trajectory	Units
	Electric energy, E_e	124.76	93.79	83.62	kJ
	Flight time, t_f	377.4	570	253.3	s
	Total mass, m	3.91	2.99	2.933	kg
Wing	Span, b_w	2.1	2.03	1.59	m
	Chord cp, c_w	0.18, 0.21	0.1, 0.1	0.1, 0.1	m
	Twist cp, θ_w	1.5, 1.5, 1.5	3.31 4.42 4.51	1.99, 4.02, 3.79	degrees
	Dihedral, $\urcorner_w$	4	4.02	3.48	degrees
	Sweep, Λ_w	1.5	1.06	0.83	degrees
	Thickness cp, t_w	0.003, 0.003, 0.003	0.0015, 0.0015, 0.0015	0.0015, 0.0015, 0.0015	m
Tail	Span, b_t	0.42	0.26	0.25	m
	Chord cp, c_t	0.14, 0.17	0.08, 0.08	0.08, 0.08	m
	Dihedral, $\urcorner_t$	0	0	0	degrees
	Sweep, Λ_t	0.5	0	0	degrees
	Thickness cp, t_t	0.0025, 0.0025, 0.0025	0.0015, 0.0015, 0.0015	0.0015, 0.0015, 0.0015	m

the best combined outcome of both.

Furthermore, we observe that less energy was spent in DP than in TP, which indicates that the initial configuration is more of a handicap to the objective of minimization than the prescribed trajectory.

We see in Tab. 7 that there was a considerable weight reduction in DP and DTP ($\approx$ 1kg) relative to the fixed configuration. This was achieved by decreasing the thickness of the spars and the size of lifting surfaces, in an effort to decrease material as much as possible, provided that stresses had a good margin to the failure limit, as verified in Fig. 6 in the plot labeled "Von Mises".

The position of the spar is coincidental with the fraction of chord of maximum (h/c), which is 10% for both surfaces, as per Tab. 1. The diameter of the spar is thus also coincidental with the maximum height of the wing's section, which means that in the same way decreasing the span leads to a reduction of the length of the spar, decreasing the chord reduces its radius. Obtaining the necessary area by increasing the span instead of the chord leads to a wing with higher aspect ratio, which yields less induced drag for a given value

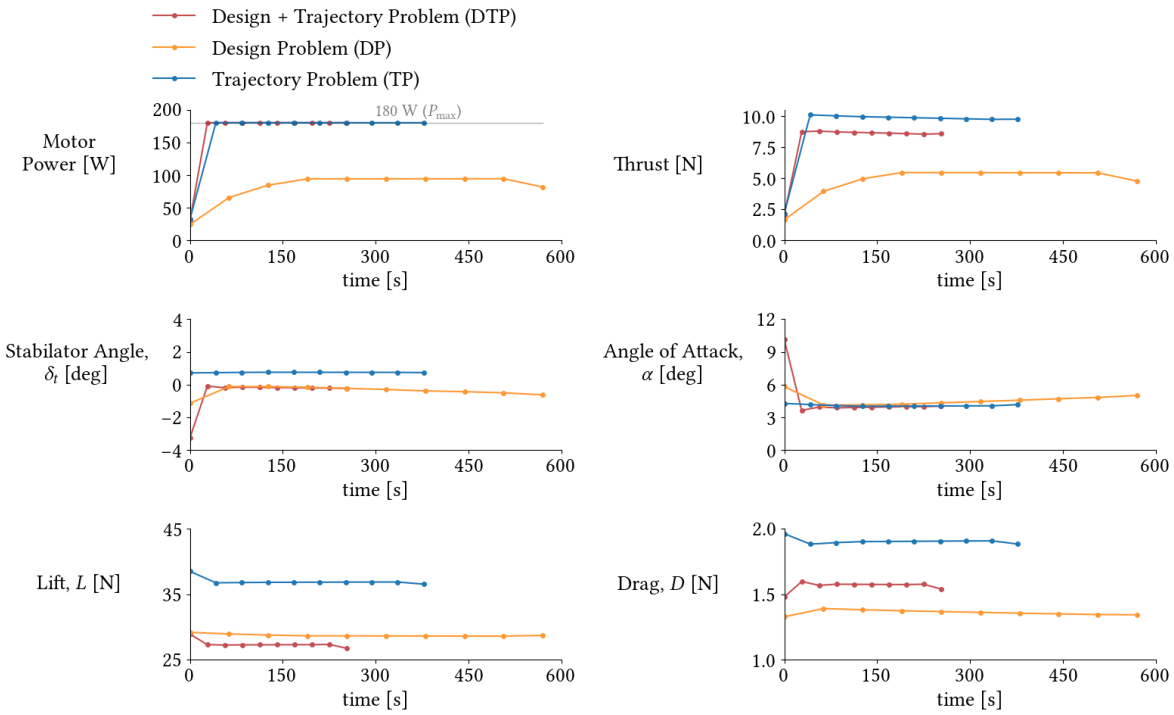

Figure 7: Results of control and trimming variables for climb energy optimization.

of lift [12].

The span of the tail was set to the lower bound in both problems. Moreover, the stabilator, which has a symmetric airfoil, had its angles set to values close to zero, as shown in the stabilator angle plot in Fig.7. These results indicate that the center o mass was brought closer to the aerodynamic center of the wing, reducing its moment, and the distance of the stabilator to the center of gravity (the arm of the tail moment) might be oversized and is the principal responsible for creating the balancing moment necessary to trim the aircraft.

The reduction of span in DTP was a 20 % greater than in DP. This can be explained by looking at the thrust and lift plots shown in Fig. 7. Because trajectory is prescribed in DP, the throttle control was chosen just to equilibrate the forces, rather than to propel the aircraft forward or increase the angle of climb. Because horizontal velocity is kept almost constant, the horizontal component of forces has to be null, and since the flight path angle is not too high, a lower thrust force was required. This means that on the vertical component, weight had to be balanced out mostly through lift. The higher lift (when compared to DTP) was achieved through a slightly higher span and twist angle, which demonstrates how a fixed trajectory penalizes the aircraft design.

The twist angles were also chosen so that lift distribution along the span would match, as closely as possible, that which corresponds to an elliptical distribution of circulation, as it minimizes C_D for a given C_L [12]. This is exemplified for DTP in Fig. 6.

Dihedral and sweep angles were changed only slightly. Dihedral's major contribution is to lateral stability, which is not accounted in this model. Likewise, sweep's main contribution is delaying divergence mach number, which is not an issue since the operational mach number is below 0.1 in all problems. The only other factor that these angles have influence in is the length of the spar. However, the angles are minimal and so this effect is of little relevance as well.

Energy spent depends directly on electric power and time, as per Eq. (9). Therefore, in order to minimize it, power or time have to be reduced. As we can see in Fig. 8, the trend was to decrease flight time as much as possible, which was achieved by shortening horizontal distance and flying faster.

To shorten the horizontal distance, it is necessary to fly with higher flight path angles, provided that vertical distance is fixed. Bearing in mind that lift's vertical component gets smaller for higher flight path angles, the burden of counteracting weight falls on thrust. To that end, throttle control was pushed to the maximum in DTP and TP. It seems counter intuitive to have power set to its limit, but the energy saved by making flights shorter surpasses the added expense of having higher power, thus yielding a positive balance and minimizing energy consumed.

The average air speed was decreased from the 15 m/s of the initial trajectory to 14.4 m/s, in TP. This can be seen as way to compensate for the large wingspan and not generate more lift than the necessary to trim the

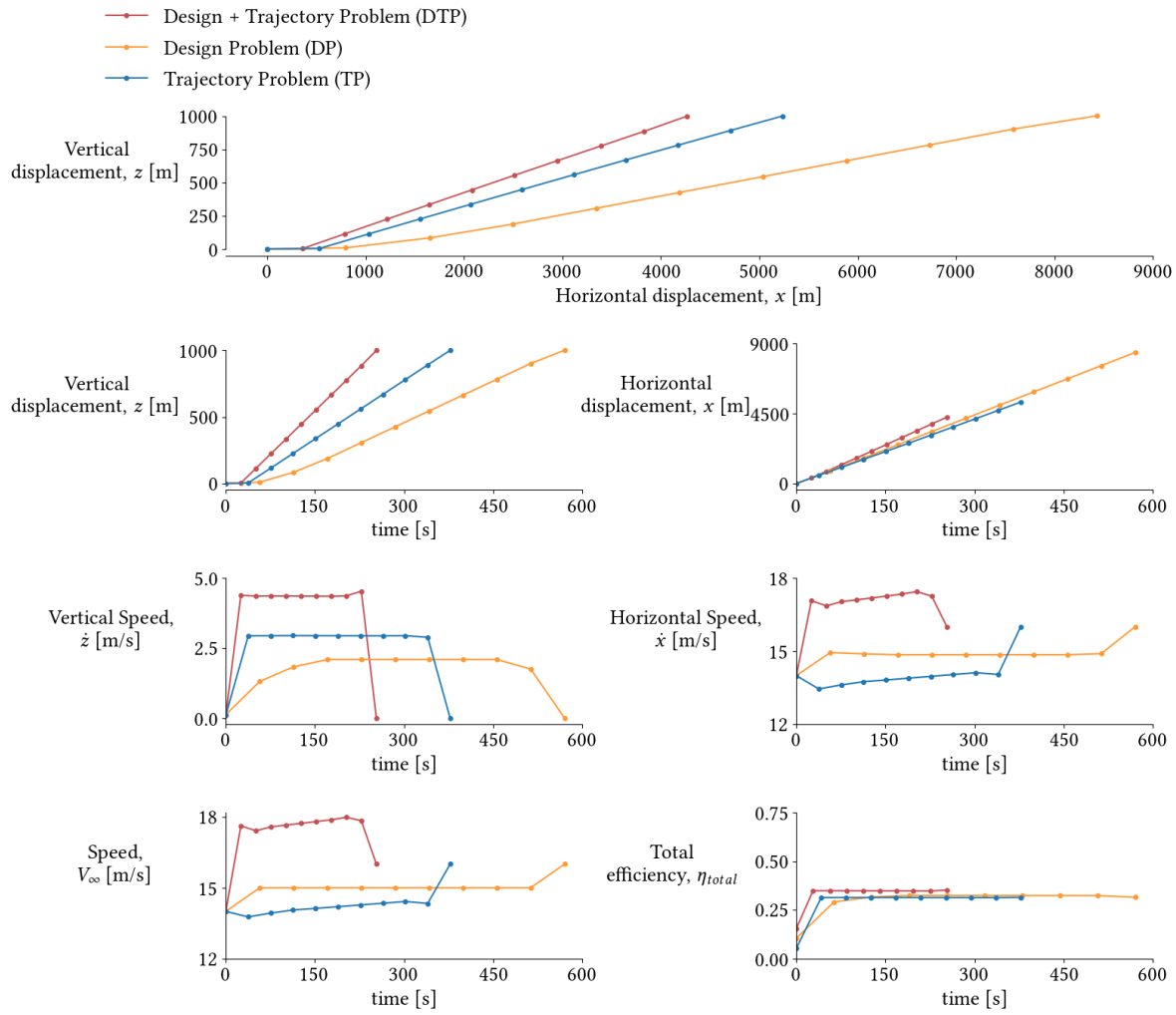

Figure 8: Results of trajectory variables for climb energy optimization.

UAV. Since DTP also optimized the configuration, the wingspan was reduced, thus allowing the speed to be increased to 17.5 m/s, on average. Although flying at higher speeds does decrease the time to cover the same distance, it also lowers thrust forces, as they are approximately inversely proportional. This limits the angle of climb and as a consequence extends horizontal distance. Therefore, the chosen speeds are an optimal balance between travelling fast and travelling less.

The trajectory in DTP had major improvements relative to that of TP, as the latter was heavily penalized by the fixed configuration. TP's larger wingspan generated a much higher lift and consequently, a higher drag and pitching moment. To comply with the zero moments constraint, the stabilator control angle was set to positive values, since the larger structural mass pulled the center of mass more in the direction of the trailing edge.

The flight path angle could not be increased as much in TP, because the aircraft design was fixed and therefore, so was weight. This greater weight was balanced mostly through lift, which was naturally much higher than in the other problems, given the larger wingspan. As described before, for greater climb angles, the vertical component of lift decreases, but, in this case, it also becomes quite significant that the horizontal component grows. Inversely, the vertical component of thrust increases and the horizontal decreases, resulting in a two way burden for thrust. The maximum power was the same for all problems and in TP it was clearly insufficient to trump weight and the horizontal component of lift at high γ. Conversely, design was also optimized in DTP, so a better trajectory was achieved through the configuration modifications previously discussed, which ultimately led to less energy spent.

This shows how the fixed design negatively impacted the trajectory optimization potential, or the other way around, how having both design and trajectory be part of the optimization led to better results.

The efficiency results are shown in Fig. 8. Efficiency is capped at 50% because that is the loss factor considered between battery and motor. The remaining losses

can be attributed to drag resistance and to the propulsive system, which performed with an efficiency of between 80% and 86%. For DTP, for example,

$$\eta_{prop} = \frac{T V_\infty}{P_m} \approx \frac{8.7 \times 17.5}{180} \approx 85.0\%. \tag{19}$$

Efficiency plots basically show how effectively electrical energy was converted into gravitational potential energy, given that variations in velocity were much smaller than those of vertical displacement. DTP had higher efficiency than the other problems, which is another evidence of how advantageous it is to have all disciplines being optimized simultaneously.

Results from Fig. 8 highlight some limitations of the discretization method employed. It is a forward Euler scheme, so the ith state and control values are used in the interval delimited by points i and $i + 1$. Initial and final states are pre defined, so the first interval uses the boundary condition value. This is not a problem in itself, but since the trajectory is parameterized by 10 intervals only, each segment lasts 10 % of the entire flight time, which is still a considerable amount of time to fly at non optimal conditions. This could be mitigated through a more refined discretization, however, not only would it increase the number of variables, it would also incur in more mission points and fluid structure calculations, which drives up the computational cost. A more efficient alternative would be using B-Splines to parameterize state and control. This would result in continuous and smooth function at the cost of few control points and therefore, fewer mission points as well.

5. Conclusions

In this work, the OpenAeroStruct framework was upgraded to accommodate an electric propulsive system and compute performance metrics relevant to such a system. Furthermore, the framework was expanded to include trajectory optimization, which was performed through the implementation of a collocation method.

Aircraft design, trajectory and coupled design and trajectory optimizations were performed for the same mission with the objective of minimizing energy. It was concluded that optimizing design and trajectory simultaneously had a great impact in achieving better results, as the isolated problems were greatly limited by the initial guesses for configuration and trajectory. The coupled optimization was able to further minimize energy in 33% and 10.8%, relative to the isolated trajectory and aircraft design optimizations. The coupled optimization was computationally more expensive, and it was also verified that the cost did not scale linearly with problem size.

References

[1] J. P. Jasa, J. T. Hwang, and J. R. R. A. Martins. Open-source coupled aerostructural optimization using Python. *Structural and Multidisciplinary Optimization*, 57(4):1815–1827, April 2018. doi: 10.1007/s00158-018-1912-8.

[2] J. S. Gray, J. T. Hwang, J. R. R. A. Martins, K. T. Moore, and B. A. Naylor. OpenMDAO: An open-source framework for multidisciplinary design, analysis, and optimization. *Structural and Multidisciplinary Optimization*, 59(4):1075–1104, April 2019. doi: 10.1007/s00158-019-02211-z.

[3] J. D. Anderson Jr. *Fundamentals of aerodynamics*. McGraw-Hill, 5th edition, 2010.

[4] B. W. McCormick. *Aerodynamics, Aeronautics and Flight Mechanics*. John Wiley & Sons, 2nd edition, 1995.

[5] S. S. Chauhan and J. R. R. A. Martins. Tilt-wing eVTOL takeoff trajectory optimization. *Journal of Aircraft*, 57(1):93–112, Jan. 2020. doi: 10.2514/1.C035476.

[6] T. J. Böhme and B. Frank. *Hybrid Systems, Optimal control and Hybrid Vehicles*. Springer International Publishing, Cham, Switzerland, 2017.

[7] G. T. Huntington and A. V. Rao. Comparison of global and local collocation methods for optimal control. *Journal of Guidance, Control, and Dynamics*, 31(2):432–436, 2008. doi: 10.2514/1.30915.

[8] A. B. Lambe and J. R. R. A. Martins. Extensions to the design structure matrix for the description of multidisciplinary design, analysis, and optimization processes. *Structural and Multidisciplinary Optimization*, 46:273–284, 2012. doi: 10.1007/s00158-012-0763-y.

[9] Z. Lyu, Z. Xu, and J. R. R. A. Martins. Benchmarking optimization algorithms for wing aerodynamic design optimization. In *Proceedings of the 8th International Conference on Computational Fluid Dynamics*, Chengdu, Sichuan, China, July 2014. ICCFD8-2014-0203.

[10] Tekever AR4 UAV. URL `http://uas.tekever.com/ar4-evo/`. [Accessed on 12/09/2020].

[11] Y. Liao, S. He, J. R. R. A. Martins, and Y. L. Young. Hydrostructural optimization of generic composite hydrofoils. In *AIAA SciTech Forum*, Orlando, FL, Jan. 2020. AIAA. doi: 10.2514/6.2020-0164.

[12] V. d. Brederode. *Aerodinâmica Incompressível: Fundamentos*. IST Press, Lisboa, 2014.